Journal of Materials Chemistry A

ROYAL SOCIETY OF CHEMISTRY

PAPER

Cite this: J. Mater. Chem. A, 2024, 12, 20238

Metal-ion exsolution effect to accelerate the reaction kinetics in Li–S batteries†

Hongxu Zhou,[a] Weichen Han,[a] Hongquan Chai,[a] Hao Huang,[a] Jingang Zheng,[a] Han Zhang, *[a] Lixiang Li, [a] Weimin Zhou,[a] Baigang An[a] and Chengguo Sun*[ab]

Sluggish reaction kinetics in lithium–sulfur (Li–S) batteries has seriously hindered their practical application. Herein, a three-dimensional (3D) granular carbon skeleton decorated with nickel-rich NCM materials (NCM@3D-SP) is prepared as a cathode host for Li–S batteries, where the carbon matrix is rich in pore channels, can provide good conductivity and electrolyte diffusion, and NCM811 particles contribute abundant metal sulfides active sites through metal-ion exsolution. The different metal sulfides (NiS, Ni_3S_2, Ni_7S_6, and CoS) in heterogeneous structures exhibit outstanding catalytic and adsorption effects on polysulfides during cycling, where the ion diffusion coefficient is increased by approximately 2.5 times compared to the cathode without catalytic active sites (3D-SP). A Li metal battery using NCM@3D-SP/S as the cathode exhibits a capacity decay of only 0.051% per cycle at 2C after 500 cycles. Even at an ultra-high current density of 10C and a sulfur-loading of 6 mg cm^{-2}, the cells maintain a stable reversible discharge capacity of 453.1 mA h g^{-1} after 500 cycles and 4 mA h cm^{-2}. The incorporation of nickel-rich cathode materials and 3D sulfur host structure presents a novel strategy for high-catalytic activity cathodes of Li–S batteries.

Received 9th May 2024
Accepted 25th June 2024

DOI: 10.1039/d4ta03248a

rsc.li/materials-a

1. Introduction

Li–S batteries are considered to be one of the most promising energy storage systems of the next generation due to their ultra-high energy density (2600 W h kg^{-1}) and theoretical specific capacity (1675 mA h g^{-1}). Both the low cost and natural abundance of sulfur produce inborn advantages for the large-scale application of Li–S batteries.[1–4] However, the poor conductivity of active materials (S_8/Li_2S) and the sluggish reaction kinetics of polysulfides during cycling have seriously impeded further practical application.[5,6]

To overcome these shortcomings, carbon materials were commonly employed as the sulfur-loaded matrix because of their excellent electron conductivity and ability to alleviate volume expansion.[7–9] The only drawback is that the void space inside carbon materials with nanostructures can absorb solvents during the cathode fabrication, which is undesirable for the slurry rheology.[10] On the other hand, the weak interaction between the carbon material and polysulfides is unable to solve the shuttle problem of lithium polysulfides (LiPSs).[11,12] Element-adopted carbon materials with various active sites have been widely adopted,[13,14] including metal oxides,[15,16] metal nitrides,[17] metal sulfides,[18,19] and so on. These polar materials provide abundant sites for LiPSs adsorption and can even enhance the efficiency of catalytic conversion to a certain extent.[20] For example, a hybrid material NiS@C-HS with nano-NiS uniformly distributed on the 3D hollow spheres as a sulfur cathode has resulted in a low capacity decay of 0.013% per cycle after 300 cycles.[21] Recently, a yolk–shell nanoreactor consisting of a nano-particle NiO-core and a conductive carbon-shell has been fabricated as metal catalytic sites to accelerate the conversion of LiPSs. Fast reaction kinetics can dramatically suppress LiPSs shuttling, with an average capacity decay of 0.06% per cycle after 300 cycles at 1C.[22] Although the above-mentioned polar materials have revealed strong interaction with LiPSs, from the multiple conversion process of sulfur, the introduction of a single substance/element catalyst always shows a limited function for the whole LiPSs adsorption and catalytic conversion.[18]

In order to meet the requirements for faster reaction kinetics, heterostructures have been widely researched due to the combination of the advantages of different components.[23] For example, in the metal-based oxygen-sulfide heterostructure, the addition of metal sulfide can compensate for the poor conductivity and weak catalytic ability of metal oxide, making the heterostructure exhibit faster reaction kinetics for LiPSs.[24] In other cases, the MoS_2–Ni_3S_2 heterostructure has been designed as a self-supported catalyst host, in which MoS_2 ensures the fast conversion of LiPSs, and Ni_3S_2 can realize LiPSs adsorption and rapid electron transfer.[18] Therefore,

[a]School of Chemical Engineering, University of Science and Technology Liaoning, Anshan, 114051, China

[b]School of Chemical Engineering, Nanjing University of Science and Technology, Nanjing, 210094, China. E-mail: sunyangguo2004@163.com

† Electronic supplementary information (ESI) available. See DOI: https://doi.org/10.1039/d4ta03248a

constructing heterostructure catalysts to realize the fast redox reaction kinetics for Li–S batteries is one of the most effective methods.

$Li(Ni_xCo_yMn_z)O_2$ (NCM) layered oxides are the most popular ternary cathode materials in lithium-ion batteries, in light of the simultaneous presence of nickel, cobalt, and manganese.[25] We conceive the application of the NCM series in Li–S batteries as multi-metal elements co-catalysis. Herein, a 3D granular carbon interconnected skeleton decorated with ternary $LiNi_{0.8}Co_{0.1}Mn_{0.1}O_2$ (NCM811) materials as a cathode carrier (NCM@3D-SP) for Li–S batteries is reported. Benefiting from the exsolution of metal ions, NCM811 contributes to the important synergistic catalysis in the conversion of LiPSs by forming a multiphase heterostructure after cycling. The multi-metal ions in NCM811 underwent ion exsolution and combination with S^{2-} during cycling to produce a series of transition metal-sulfides on the cathode surface. The high catalytic activity of the above metal sulfides for polysulfide improves the reaction kinetics of the cathode. After assembling the Li–S battery, the capacity decay of the NCM@3D-SP/S cathode is only 0.051% per cycle at 2C after 500 cycles. Even at the ultra-high current density of 10C, it still maintains a stable reversible discharge capacity of 453.1 mA h g^{-1} after 500 cycles. Furthermore, depending on the synergistic effect between the porous 3D conductive skeleton and NCM811, a high areal capacity of 4 mA h cm^{-2} for the NCM@3D-SP/S cathode was achieved under a high sulfur-loading of 6 mg cm^{-2} and low E/S ratio of 7 μL mg^{-1}. The results suggest that the application of NCM811 in Li–S batteries is a promising strategy for realizing fast reaction kinetics, high current density, and areal capacity.

2. Experimental section

2.1 Preparation of NCM@PEO-SP

Acetonitrile was mixed with a 3 : 2 mass ratio of PEO (average Mw 4 000 000) and Super P (SP) until the mixture was viscous and particle-free; for the amount of NCM811 added, we attempted 5 wt%, 10 wt%, 20 wt%, 40 wt%, and 60 wt% as shown in Fig. S18,† of which 10 wt% was considered to be optimal and used in all other characterization studies.

After adding NCM811 and stirring for about 2 h, the homogeneous slurry was casted on a carbon paper collector and vacuum dried at 60 °C for 12 h to obtain the PEO-SP material loaded with uniformly dispersed NCM811 particles (NCM@PEO-SP).

2.2 Preparation of NCM@3D-SP

A typical high-temperature calcination method was used to prepare the NCM@3D-SP framework. The previously prepared NCM@PEO-SP material was punched into 12 mm diameter disks, which were placed into a porcelain boat and calcinated at 600 °C for 2 h under an Ar atmosphere. A three-dimensional carbon material framework with loaded NCM811 (NCM@3D-SP) was obtained after cooling. For comparative analysis, various monometallic lithium salts, such as $LiMn_2O_4$, $LiNiO_2$, and $LiCoO_2$ were loaded in the 3D carbon material frameworks named LMO@3D-SP, LNO@3D-SP, and LCO@3D-SP.

2.3 Preparation of NCM@3D-SP composite sulfur

A melt-diffusion strategy was used for sulfur loading. First, S/CS_2 solution with a specific concentration of 30 mg mL^{-1} was prepared, and 30 μL was dropped onto the NCM@3D-SP electrodes (ϕ 12 mm) after the complete dissolution of sulfur. The electrodes were left to allow the complete volatilization of CS_2, then heated at 155 °C for 3 h under an Ar atmosphere to ensure a uniform distribution of sulfur. The resulting material was named NCM@3D-SP/S. The sulfur loading was determined by weighing the mass before and after the loading process. The area loading of sulfur was 1–1.3 mg cm^{-2}.

2.4 Materials and characterization

All chemicals were directly used without purification. Li–S electrolyte (LS-009, Suzhou Duoduo Chemical Technology Co.), PEO (Mw 4 000 000, Sigma-Aldrich), commercial NCM cathode material (NCM811), Super P conductive carbon black, and single metal cathode materials (LNO, LCO and LMO, Kejing Zhida Technology Co.), sulfur (S_8, Aladdin), carbon paper (CP, Suzhou Sinero Technology Co.).

The microstructure and morphologies of the samples were analyzed by scanning electronic microscopy (SEM, Thermo Fisher Scientific Apreos) and transmission electron microscopy (TEM, Tecnai G2 F30 S-TWIN). Energy dispersive X-ray (EDX) spectroscopy was performed with an EDAX EDX-Detector to determine the composition of the cathode. The thermogravimetric analysis measurements were conducted using a Rigaku TG-DTA 8122 simultaneous thermal analyzer with a heating rate of 10 °C min^{-1} from room temperature to 800 °C in an air atmosphere. The X-ray photoelectron spectroscopy (XPS) was performed using an Axis-Supra, Kratos. Raman spectra were recorded using a LabRAM HR Evolution, HORIBA.

2.5 Electrochemical measurements and characterization

The electrochemical activity of liquid batteries assembled with different cathodes was evaluated. The CR-2025-type coin cells were assembled in a glove box under an Ar atmosphere. The electrolyte consisted of DOL (1,3-dioxolane) and DME (1,2-dimethoxyethane) (1 : 1, volume ratio), dissolved with 1 M LiTFSI and 0.1 wt% $LiNO_3$. The cells were assembled using one piece of Li metal as the anode and a Celgard 2500 as the separator, filled with 25 μL Li–S electrolyte, and then sealed. Additionally, a cathode with a high areal sulfur loading of 6 mg cm^{-2} was assembled using the same method, filled with 20 μL Li–S electrolyte (E/S = 7 μL mg^{-1}). The cells were galvanostatically cycled between 1.7 and 2.8 V using a Land battery test system at different C-rates (1C = 1675 mA g^{-1}). Cyclic voltammetry (CV) curves were recorded from 1.7 to 2.8 V at different scan rates (0.1–0.5 mV s^{-1}) using a BioLogic VSP-300. Electrochemical impedance spectroscopy (EIS) was conducted with an AC signal of an amplitude of 10 mV and a frequency range of 0.01 Hz to 100 kHz at room temperature.

2.5.1 Polysulfide shuttling test. To prepare the S/SP cathode for comparison, a mixture of 60 wt% sulfur, 30 wt% Super P, and 10 wt% PVDF in *N*-methyl-2-pyrrolidone (NMP) was stirred to form a uniform slurry. The slurry was coated onto an aluminum foil collector and vacuum-dried at 60 °C overnight to form the working electrode. The transparent batteries were assembled by using NCM@3D-SP/S and S/SP as cathodes, the anodes were both lithium foil and matched with the Li–S electrolyte. During the initial discharge process, photos were taken to record the color change of the solution.

2.5.2 Synthesis of Li_2S_6 and Li_2S_8 solution. Sulfur and Li_2S were mixed at a molar ratio of 5 : 1, followed by magnetically stirring with a mixture of a certain amount of LiTFSI, DOL, and DME (1 : 1 by volume ratio) under Ar at 70 °C until turning dark brown, and the Li_2S_6 solution was obtained. The Li_2S_8 solution was made in the same way as before, except that the molar ratio of S and Li_2S was changed to 7 : 1.

2.5.3 Measurement of the Li_2S nucleation. NCM@3D-SP, LNO@3D-SP, LMO@3D-SP, and LCO@3D-SP were used as the cathodes, and lithium foil as the anode. 25 μL Li_2S_8 (0.2 M) solution was added to the cathode side, and the electrolyte without Li_2S_8 was added into the anode side. The batteries were galvanostatically discharged to 2.06 V at 0.112 mA and potentiostatically held at 2.05 V until the current decreased below 10^{-5} A.

2.5.4 Symmetrical cells of Li_2S_6. Each symmetric cell consisted of the same materials used as the working electrode and the counter electrode with 20 μL Li_2S_6 electrolyte on each side. CV and Tafel tests were performed on each symmetric cell.

2.5.5 Measurement of GITT. A protocol of a current pulse at 0.1C for 20 min with 20 min of rest was used. The degree of polarization in the discharge and charge processes can be judged according to the value of $\Delta R_{\text{internal}}(\Omega)$, referring to the following relationships:

$$\Delta R_{\text{internal}}(\Omega) = |\Delta V_{\text{QOCV-CCV}}|/I_{\text{applied}}$$

where $\Delta V_{\text{QOCV-CCV}}$ represents the potential difference between the quasi-open-circuit voltage (QOCV) and closed-circuit voltage (CCV), and I_{applied} represents the applied current (inset in Fig. 3e and S17†).

2.5.6 Calculation of lithium-ion diffusion coefficient. The lithium-ion diffusion coefficient can be calculated from CV curves and the EIS impedance spectrum. First, the linear relationship between peak current density (I_{peak}) and square root scanning rate can be obtained through the CV curves, referring to the Randles–Sevcik equation:

$$I_{\text{p}} = (2.65 \times 10^5) n^{1.5} S {C_{\text{Li}^+}}^{0.5} \Delta C_{\text{Li}^+} v^{0.5}$$

where n represents the charge transfer number, S represents the area of one side of the electrode, D_{Li^+} is the Li ion diffusion coefficient, and ΔC_{Li^+} is the concentration of Li^+.

Furthermore, the Z' and $\omega^{-0.5}$ of the batteries after 50 cycles were also calculated through the EIS spectrum to obtain the lithium ion diffusion coefficient, based on the following equation (Tables S3 and S5†):

$$Z' = R_{\text{s}} + R_{\text{ct}} + \sigma\omega^{-0.5}$$

$$D_{\text{Li}^+} = \frac{R^2T^2}{2A^2n^4F^4{C_{\text{Li}^+}}^2\sigma^2}$$

where D_{Li^+} represents the Li^+ diffusion coefficient, R is the gas constant, T is the room temperature, A is the electrode area, n is the electron transfer number, F is the Faraday's constant, C_{Li^+} is the Li^+ concentrate and σ represents the slope value obtained by fitting Warburg's constant Z' and the angular frequency ω.

3. Results and discussion

3.1 Material characterization

The formation of NCM@3D-SP by simple vacuum and carbonization processes is shown in Fig. 1a. First, the slurry containing NCM811, PEO, and SP was coated on the carbon paper collector, and NCM@PEO-SP was obtained by drying under vacuum. Afterward, NCM@PEO-SP was carbonized at 600 °C under an Ar atmosphere to form a granular 3D carbon skeleton, consisting of tandem SP particles and loaded with NCM811 particles. The morphology and structure of the final product NCM@3D-SP were examined by scanning electron microscopy (SEM) and high-resolution transmission electron microscopy (HRTEM). Fig. 1b illustrates the tandem SP post-carbonization, due to the removal of PEO, the SP skeleton exhibits porosity and a granular 3D structure. The cross-sectional SEM images of 3D-SP and NCM@3D-SP (Fig. S1 and S2†) further confirm that their internal structures are the same porous structures as those shown in Fig. 1b. The NCM811 particles were uniformly dispersed on the 3D-SP, indicating successful implantation of NCM811 in the carbon skeleton (Fig. 1c and d). Moreover, the introduction of NCM811 particles can improve the slurry rheology,[10] resulting in a denser and more uniform cathode (Fig. S3†). Due to the advantage of the rich pores within the 3D skeleton, the electrolyte efficiently infiltrates the electrode, as evidenced by the reduced contact angle in Fig. S4.† The HRTEM image of NCM@3D-SP is shown in Fig. 1e, revealing that the surface of NCM811 is a (111) crystal facet exposed rock salt phase and covered by a thin carbon layer. This is due to the high Ni content of NCM811 particles, which is more prone to forming oxygen vacancies during the thermal induction (Fig. S5†), leading to the severe degradation of the lattice structure evolving into a rock salt phase.[26] Also, the CO and CO_2 produced by PEO during carbonization were released, while the remaining carbon fell on the 3D skeleton to form a uniform carbon layer. Additionally, the carbon content of the NCM@3D-SP electrode was determined *via* TGA. As shown in Fig. S6,† the thermal weight loss period was used to determine the carbon content, which was found to be 79.54%, indicating excellent conductivity of the sample. The Raman spectrum of NCM@3D-SP exhibits distinct D and G bonds at 1352 and 1580 cm^{-1}, respectively (Fig. 1f). The D peak corresponds to defects in symmetrical hexagonal graphite, and the symmetric C–C bonds of graphitic carbon are associated with the G peak.[23] The high I_D/I_G value of 1.32 indicates that NCM@3D-SP possesses more

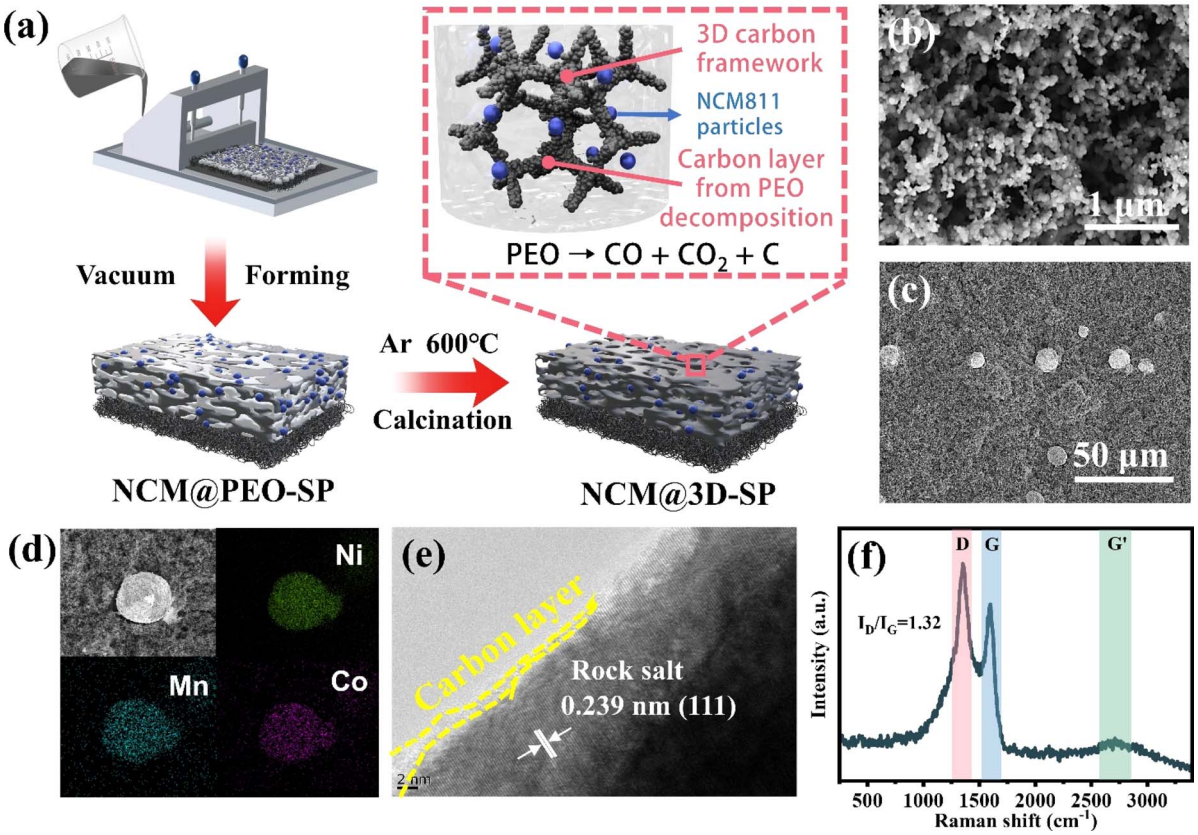

Fig. 1 (a) Schematic illustration of the fabrication process of NMC@3D-SP. Morphological and structural characterization of the synthesized nanocomposites. SEM images of (b) 3D-SP and (c) NCM@3D-SP. (d) EDX elemental mapping of NCM@3D-SP, showing elements C, Ni, Co, Mn, and O, respectively. (e) TEM and (f) Raman spectra of NCM@3D-SP.

defects and disordered structures.[27] The asymmetric wide peak of G′ at 2700 cm^{-1} suggests the stacked structure of the 3D skeleton.[28] The above results collectively suggest that the unique 3D carbon skeleton of NCM@3D-SP can enhance sulfur loading and mitigate cathode volume expansion during cycling, as well as provide abundant catalytic sites for the rapid conversion of LiPSs due to the introduction of NCM811 particles.

3.2 Electrochemical characterization

To evaluate the catalytic ability of the NCM@3D-SP for LiPS conversion, symmetric cells with various electrodes utilizing Li_2S_6 solution as the active material were assembled. As shown in Fig. S7,† in comparison to the electrode with only SP, the NCM@3D-SP electrode demonstrates two distinct pairs of redox peaks and a higher current response, indicating the enhanced catalytic ability of NCM811.[29] To further demonstrate the effectiveness of NCM811 as a heterogeneous multi-metal catalyst for LiPS conversion, the 3D electrodes loaded with monometallic catalysts (LNO@3D-SP, LCO@3D-SP, and LMO@3D-SP) were subjected to the same test for comparison. As seen in Fig. 2a, the NCM@3D-SP electrode displays two distinct pairs of redox peaks at a voltage window from −1.0 to 1.0 V, corresponding to the sequential reduction (oxidation) process of S_8 (Li_2S) to Li_2S (S_8). Significantly, the NCM@3D-SP electrode shows higher current response and narrower peak spacing, indicating the superior ability to enhance the redox kinetics of sulfur.[30] The whole sulfur redox process features were further analyzed to investigate the catalytic activity of various cathodes. The Tafel slopes were determined from the CV curves of Li–S cells with different cathodes in Fig. S8.† Compared to the other three hosts, the NCM@3D-SP electrode exhibits the lowest Tafel slopes of 70.43 mV dec^{-1} and 18.26 mV dec^{-1} for oxidation and reduction processes (Fig. 2b and c), respectively, indicating perceptible kinetic promotion of sulfur species during charging and discharging. To further prove the aforementioned conclusions, the optical images of polysulfide shuttle are presented in Fig. S9† at varied discharge times; the NCM@3D-SP/S cathode only exhibits a light-yellow color after 120 minutes of discharge (Fig. S9a†). In contrast, the S/SP cathode suffered a severe shuttling effect after 120 minutes, and the electrolyte displayed a dark yellow color (Fig. S9b†).

The overpotential of nucleation for Li_2S was further investigated as shown in Fig. 2d. The NCM@3D-SP cathode reveals the lowest Li_2S nucleation overpotential of 13 mV compared to LNO@3D-SP (24 mV), LMO@3D-SP (42 mV), and LCO@3D-SP (50 mV). The higher overpotential during discharging indicates a higher energy barrier for Li_2S nucleation, the above results consistent with the reaction dynamics depicted in Fig. 3. Chronoamperometry technology was employed to observe the nucleation process of Li_2S. The potentiostatic current profiles of

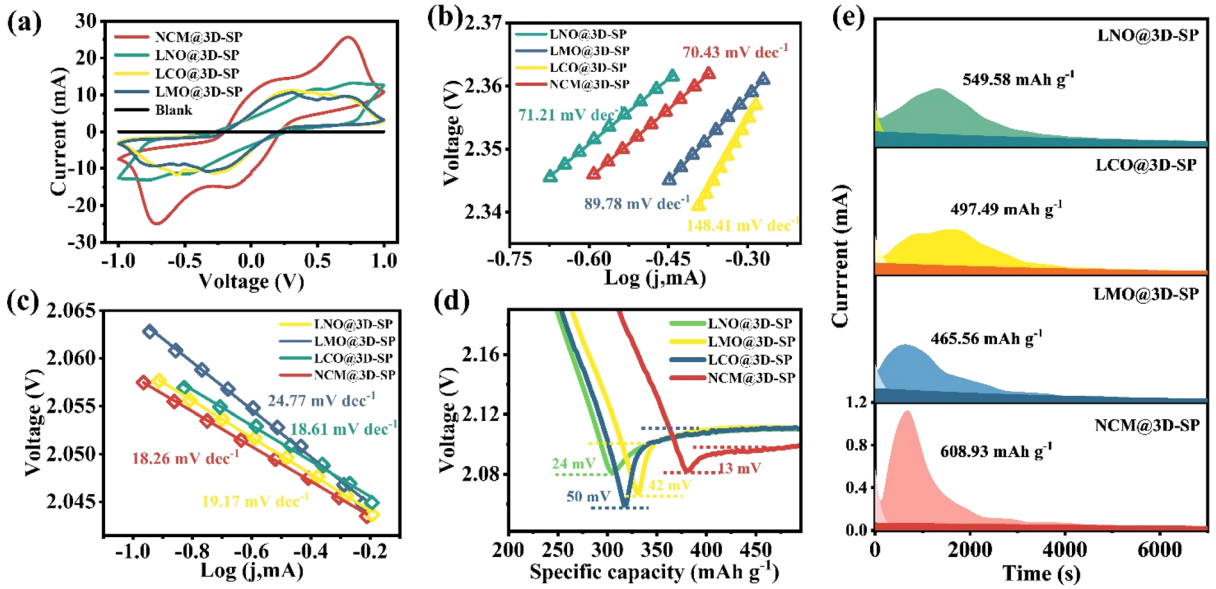

Fig. 2 Evaluation of the electrocatalytic activities of Li–S batteries. (a) Cyclic voltammetry profiles of Li_2S_6 symmetric cells with different cathodes. Tafel plots of (b) oxidation and (c) reduction processes. (d) Overpotentials of the reduction process while the different electrodes were being discharged. (e) Curves representing potentiostatic deposition of Li_2S on different electrode surfaces.

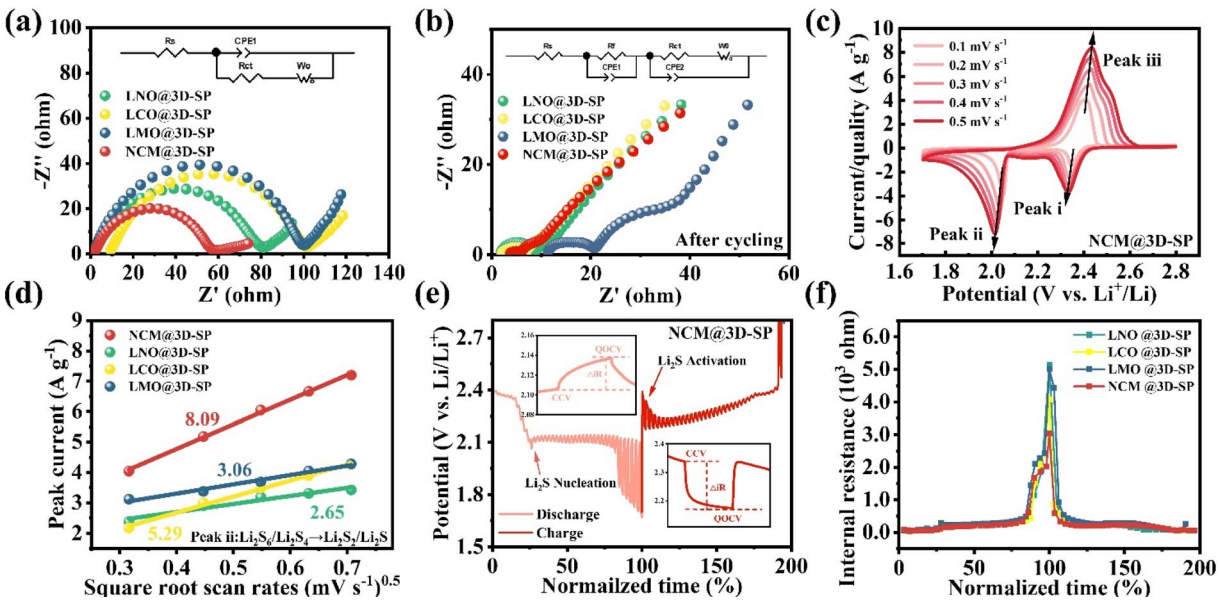

Fig. 3 Evaluation of the Li-ion diffusion of Li–S batteries. (a) EIS diagram before the cycle and (b) EIS diagram after cycling of different cathodes. (c) CV profiles at different scan rates of NCM@3D-SP and (d) corresponding *I*–*V*-0.5 slope curves at peak ii. (e) GITT voltage profiles of NCM@3D-SP at 0.1C and (f) internal resistance of different electrodes relative to the normalized discharge–charge time.

Li_2S precipitation on various cathode surfaces are shown in Fig. 2e. By activating the nucleation and growth process of Li_2S, the long-chain LiPSs were initially discharged to 2.06 V and subsequently held at 2.05 V.[31] According to Faraday's law and the quantity of active materials in various electrodes,[32] the Li_2S precipitation capacities were calculated. The Li_2S deposition capacity of the NCM@3D-SP electrode (608.93 mA h g^{-1}) was higher than that of LNO@3D-SP (549.58 mA h g^{-1}), LCO@3D-SP (497.49 mA h g^{-1}), and LMO@3D-SP (465.56 mA h g^{-1}). It is shown that the NCM@3D-SP system possesses high electrochemical activity and robust nucleation kinetics for Li_2S precipitation. To directly observe the enhancement of the reaction kinetics resulting from the introduction of NCM811, SEM and X-ray photoelectron spectroscopy (XPS) tests were conducted on the cathodes and separator after cycling (Fig. S10 and S11†). The virtual absence of dendrites and reduced polysulfides across the separator indicate the excellent capacity of the NCM@3D-SP system to catalyze conversion and mitigate the

shuttling of LiPSs. These findings demonstrate that NCM811 as a multi-metal additive can reduce the energy barrier for Li_2S nucleation and enhance the kinetics of LiPS conversion.

The virtual absence of dendrites and reduced polysulfides across the separator indicate the excellent capacity of the NCM@3D-SP system to catalyze conversion and mitigate the shuttling of LiPSs. These findings demonstrate that NCM811 as a multi-metal additive can reduce the energy barrier for Li_2S nucleation and enhance the kinetics of LiPSs conversion.

3.3 Electrochemical performance of the Li–S batteries

In addition to effective catalytic conversion, rapid ion diffusion of the cathode is crucial for providing superior electrochemical performance to batteries. To investigate variations in the charge transfer mechanism of cells with different cathodes, electrochemical impedance spectroscopy (EIS) tests were employed before and after cycling at 0.1C. The Nyquist plots before cycling and the corresponding fitted equivalent circuit diagram are displayed in Fig. 3a. All tested cells exhibit a semicircle in the high-frequency region and a sloped line in the low-frequency region. The fitted results reveal that the NCM@3D-SP cathode exhibits the lowest charge transfer resistance (R_{ct}) value among the other cells (Table S1†), suggesting that the NCM811 particles function as a rapid ionic conductor within the cathode, facilitating the rapid transfer of Li^+ to the active materials and mitigating ion transport resistance. However, a new high-frequency region semicircle (R_f) appeared after 100 cycles at 0.2C, due to the development of a Li_2S/Li_2S_2 deposition layer on the electrode surface (Fig. 3b), the corresponding lattice spacing was observed in Fig. S12.† As shown in Table S2,† the R_f and R_{ct} values of the NCM@3D-SP/S cathode are the smallest compared with the other electrodes.

These results further demonstrate the efficient conversion of LiPSs by the NCM811 particles, inhibiting the irreversible deposition of electron/ion-insulating discharge products (Li_2S/Li_2S_2). The Li^+ diffusion coefficients (D_{Li^+}) for various cathodes were calculated and are presented in Table S3.† The NCM@3D-SP cathode displays the highest D_{Li^+} (7.86×10^{-11} cm^2 s^{-1}). To highlight the enhancement of the ion diffusion coefficient within the battery by NCM811 particles, the 3D-SP cathode without any additives was used for comparison. Through the Nyquist plots (Fig. S13†) and the calculated D_{Li^+} (Tables S4 and S5†) of the 3D-SP electrode, NCM can increase the diffusion coefficient in the battery system by approximately 2.5 times. The above results are also supported by the lowest internal resistance ($\Delta R_{internal}$) curve (Fig. S14†) derived from the galvanostatic intermittent titration (GITT) voltage profiles.

To further confirm the above results, the Li^+ diffusion ability for various degrees of redox processes was extensively investigated through CV curves (Fig. 3c). Compared with other tested cathodes (Fig. S15†), the NCM@3D-SP/S electrode exhibits the highest ion diffusion coefficient in all redox peaks, with slopes of 5.74, 8.06, and 11.28 (Fig. 3d, S16a, and b†) for peak i, peak ii, and peak iii, respectively. GITT voltage profiles were further measured to comprehensively analyse the internal resistance of cells with various cathodes (Fig. S17†). The NCM@3D-SP/S cathode (Fig. 3e) exhibits lower discharge/charge polarization voltage plateaus compared to the other three electrodes. Data in Fig. 3f reveal that the NCM@3D-SP/S electrode can maintain the $\Delta R_{internal}$ throughout the discharge/charge process, suggesting rapid nucleation and activation of Li_2S within the NCM@3D-SP/S electrode. Considering the above results, it is reasonable to propose that the low internal resistance and high D_{Li^+} may originate from the formation of immobilized ion channels after cycling.

To investigate the feasibility of our design for various cathodes in Li–S batteries, the optimal amount of the NCM811 additive was initially determined. As depicted in Fig. S18,† the best performance was achieved when the NCM811 additive amount was 10 mg. Subsequently, with all additives dosed at 10 mg, the electrochemical performance of the NCM@3D-SP/S, LNO@3D-SP/S, LCO@3D-SP/S, and LMO@3D-SP/S cathodes with sulfur loading of 1–1.3 mg cm^{-2} was comprehensively analyzed. Fig. 4a displays the charge/discharge curves of NCM@3D-SP/S at various rate capabilities. Notably, the curve exhibits two discharge plateaus and one charge plateau, which is characteristic of the typical charging and discharging curves observed in conventional Li–S batteries, indicating the remarkable redox reaction kinetics of LiPSs in the NCM@3D-SP/S cathode. In contrast, the other three cathodes demonstrate rapid capacity decay upon increasing the current density (Fig. S19†), due to the lack of fast catalytic conversion for polysulfides. This conclusion is supported by Fig. 4b, which shows the galvanostatic discharge/charge profiles at 0.3C for all electrodes. The NCM@3D-SP/S cathode displays the lowest polarization voltage (180 mV) among all electrodes, further supporting the above inferences. The discharge specific capacity of the NCM@3D-SP/S cathode is 1109 mA h g^{-1}, significantly exceeding that of LNO@3D-SP/S (959.3 mA h g^{-1}), LCO@3D-SP/S (834.5 mA h g^{-1}), and LMO@3D-SP/S (667.6 mA h g^{-1}). As depicted in Fig. 4c and d, the rate capacities and long-term cycling performances of Li–S batteries with various cathodes were evaluated. The steady reversible capacities of NCM@3D-SP are 1373.0, 1148.0, 990.4, 927.3, and 772.8 mA h g^{-1} at 0.1, 0.3, 0.5, 1, and 3C, respectively. Even at a high current rate of 5C, it still maintains a notable capacity of 649.5 mA h g^{-1}. Upon cycling back to 0.1C, the reversible capacity recovers to 1143.0 mA h g^{-1}, indicating the superior structural stability and electrochemical reversibility of the NCM@3D-SP/S cathode. In contrast, the other three cathodes exhibit relatively poor reversible capacities. Fig. 4d compares their long-term cycling performance at a high current rate of 2C. After 500 cycles, the NCM@3D-SP/S cathode possesses a minimal capacity decay of 0.051% per cycle and a coulombic efficiency of 99.2%, significantly outperforming LNO@3D-SP/S (0.074%), LCO@3D-SP/S (0.066%), and LMO@3D-SP/S (0.067%). Besides, Table S6† compares the performance of various cathodes in Li–S batteries from recently published articles. It can be seen that the NCM@3D-SP/S cathode still exhibits significant performance in terms of high rates and inhibition of capacity decay. The above results further confirm the advantages of the synergistic effect between the homogeneous multi-metal catalyst NCM811 and the 3D carbon skeleton for the entire redox process, thereby

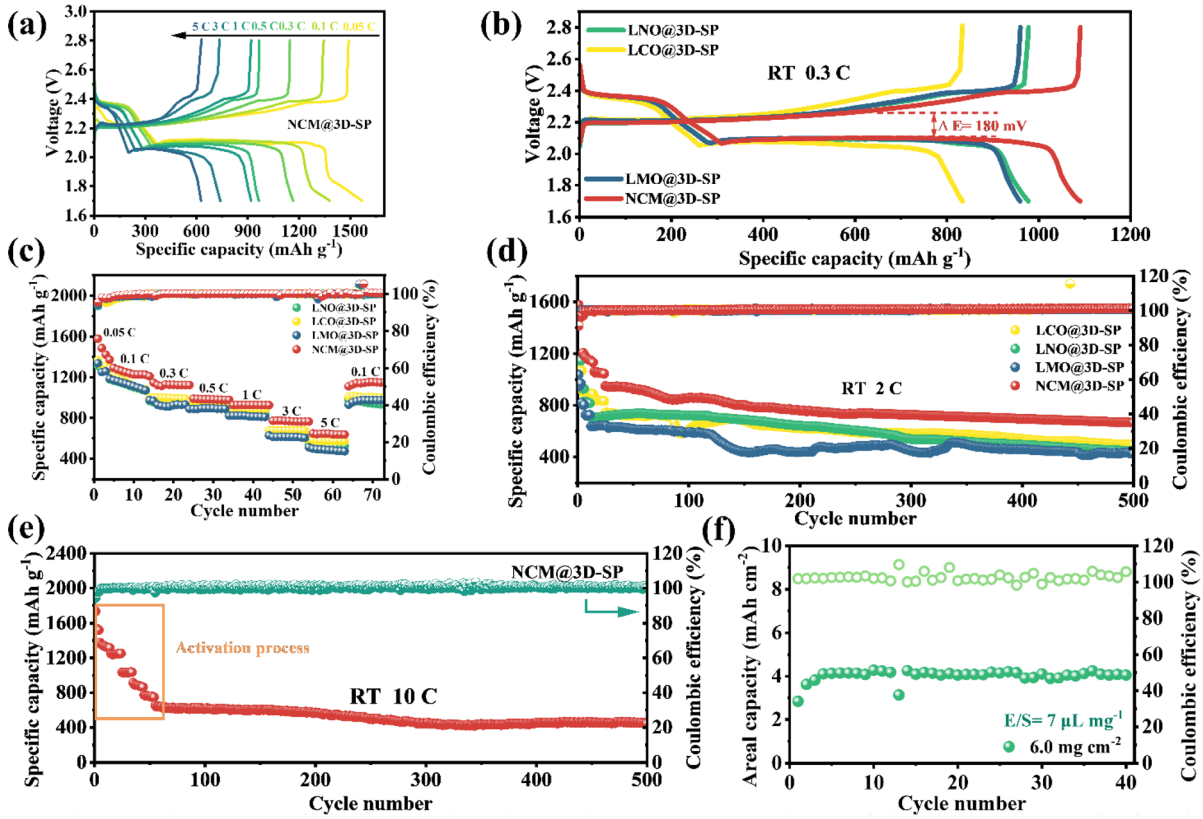

Fig. 4 Electrochemical performance of Li–S batteries with various electrodes. Charge/discharge curves of NCM@3D-SP (a) at different rate capabilities and (b) 0.3C. (c) Rate performance of different electrodes and (d) long-time cycling performance at 2C. Cycling performance of NCM@3D-SP at (e) high rate, and (f) high sulfur loading.

efficiently enhancing the reaction kinetics and sulfur utilization.

Considering the critical requirements for practical Li–S battery applications, the electrochemical performance of the cells utilizing the NCM@3D-SP/S cathode with high current density and sulfur loading was investigated. The NCM@3D-SP/S cathode provides a stable reversible discharge capacity of 453.1 mA h g^{-1} with a higher coulombic efficiency of 99.9% even at 10C for 500 cycles (Fig. 4e). On increasing the sulfur loading to 3 mg cm^{-2} and 6 mg cm^{-2}, even under a lean electrolyte (E/S = 7 μL mg^{-1}), the NCM@3D-SP/S cathode still exhibits a high areal capacity of approximately 2 mA h cm^{-2} at 0.5C after 100 cycles (Fig. S20†) and 4 mA h cm^{-2} after 40 cycles at 0.1C (Fig. 4f). These results clearly suggest that NCM811 exhibits excellent competitiveness as an efficient sulfur electrocatalyst for Li–S cathodes.

3.4 Mechanistic investigation of the NCM@3D-SP to improve the electrochemical performance of Li–S batteries

To elucidate the intrinsic reasons for the enhancement of cathode performance for the introduction of NCM811, HRTEM and XPS tests were conducted on cathode surfaces after cycling. The observed changes in the cathode after 200 cycles provide evidence that the NCM811 particles exhibit metal-ion exsolution behavior during cycling. As depicted in Fig. 5a and b, nickel and cobalt ions were initially discussed due to their higher activity. These ions underwent electrochemical reactions with S^{2-} generated during the reaction process through ion exsolution, resulting in the formation of corresponding metal-sulfides such as NiS, Ni_3S_2, Ni_7S_6, and CoS.[33,34] All of the transition metal sulfides exhibit high catalytic activity for LiPSs and rapid reaction kinetics, which can explain the superior performance of the NCM@3D-SP/S cathode. Furthermore, a lattice spacing related to Ni was also observed, which is attributed to the discharge of Ni_3S_2.[33] All the above results are supported by Ni 2p, Co 2p, and S 2p XPS spectra of the NCM@3D-SP/S cathode after 200 cycles (Fig. 5c, S21 and S22†). Besides the peaks corresponding to metal sulfides and various polysulfides observed in S 2p XPS spectra, peaks associated with S–C bonds at 165.2 eV ($2p_{1/2}$) and 163.8 eV ($2p_{3/2}$) were detected, indicating the strong interaction between metal-sulfides and carbon matrix. Due to the relative stability and low content of manganese ions in NCM811, no relevant sulfides were detected in HRTEM and XPS analyses. In addition, the NCM811 particles remained intact with a spherical structure after cycling (Fig. S23†), with the element S present in the interior. This further proves that the structure of NCM811 particles does not collapse during metal-ion exsolution, playing a decisive role in maintaining their catalytic performance.

The proposal of ion exsolution and the formation of transition metal sulfides during cycling further confirm the

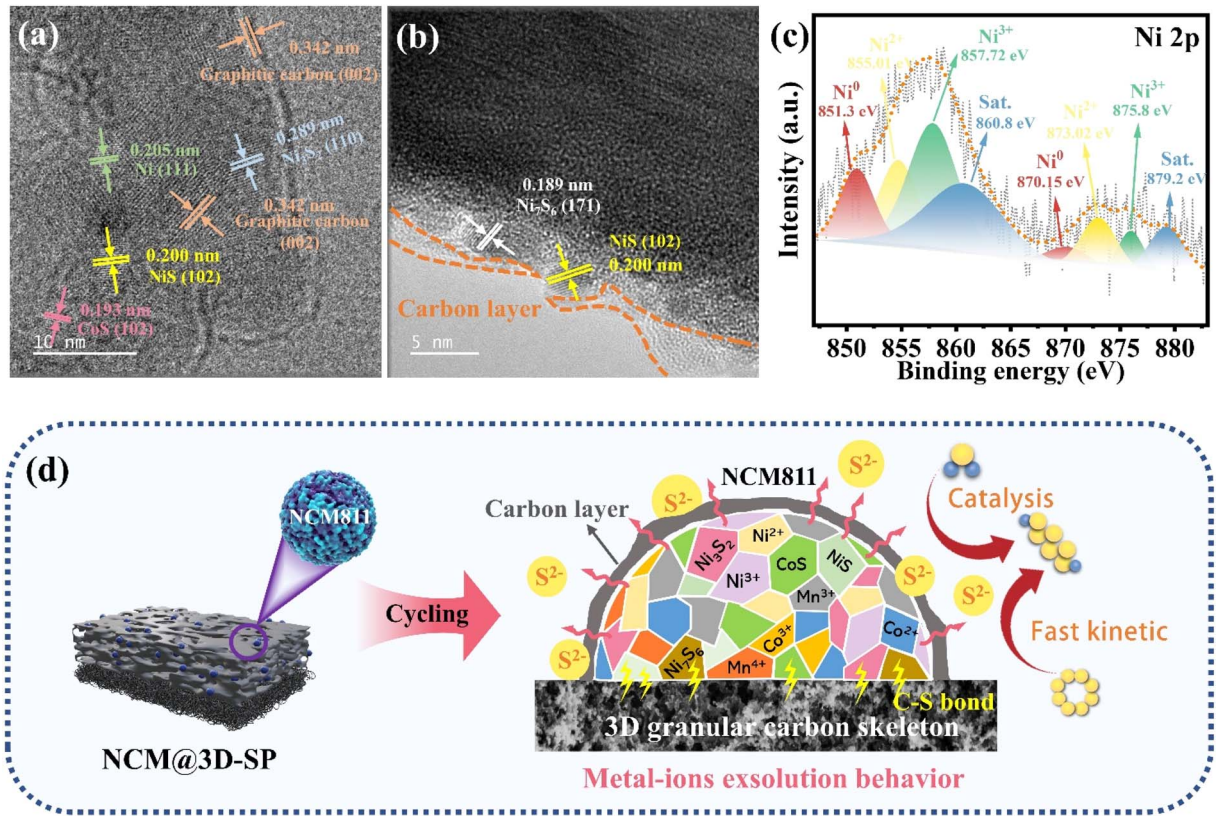

Fig. 5 (a and b) HRTEM of the NCM@3D-SP/S cathode after 200 cycles at different positions. (c) Ni 2p XPS spectra of the NCM@3D-SP/S cathode after cycling. (d) Schematic diagram of metal-ion exsolution in the NCM@3D-SP electrode during cycling.

association of NCM811 introduction with the catalysis of LiPSs and improvement of reaction kinetics. As can be seen in Fig. 5d, owing to the metal-ion exsolution behavior of NCM811 during cycling, its resulting multiphase heterogeneous structure acts as a catalyst, cooperatively catalyzing the conversion of LiPSs to further improve the reaction kinetics within the cells. This can be reasonably explained by all the characterization studies.

4. Conclusion

In this work, a 3D granular skeleton of tandem SP decorated with a small amount of ternary material NCM811 (NCM@3D-SP) was designed, serving as the cathode host for lithium–sulfur batteries. The highly conductive 3D carbon skeleton acts as an effective sulfur host, enhancing cathode loading and physically restraining the shuttling of LiPSs to a certain extent. The attached NCM811 particle plays a crucial role in the conversion of LiPSs, where the exsolution of metal ions and electrochemical reactions promote the formation of various transition metal sulfides during battery cycling. Based on the multiphase heterostructure catalyst, the cells equipped with the NCM@3D-SP/S cathode exhibit a reversible capacity of 649.5 mA h g^{-1} at 5C, and a capacity decay of 0.051% per cycle at 2C after 500 cycles. Furthermore, it can maintain a stable reversible discharge capacity of 453.1 mA h g^{-1}, even under an ultra-high current density of 10C for 500 cycles. Hence, the Li–S batteries with the NCM@3D-SP/S cathode achieve a high areal capacity of approximately 4 mA h cm^{-2} under high loading (6 mg cm^{-2}) and low E/S ratio (7 μL mg^{-1}). This strategy provides novel insights into the design of highly loaded and efficient transition metal sulfide electrocatalysts for Li–S batteries.

Data availability

The data supporting this article have been included as part of the ESI.†

Author contributions

Hongxu Zhou: investigation, data curation, writing – original draft, writing – review & editing. Weichen Han: methodology, validation, investigation. Hongquan Chai, Hao Huang, and Jingang Zheng: supervision, review & editing. Lixiang Li, Weimin Zhou, and Baigang An: project administration, writing – review & editing. Han Zhang: conceptualization, project administration, validation, writing – review & editing. Chengguo Sun: writing – review & editing, supervision, project administration, resources.

Conflicts of interest

There are no conflicts to declare.

Acknowledgements

The authors gratefully acknowledge the financial support from the National Natural Science Foundation of China (11972178, 51972156 and 22109061), the Nature Science Foundation of Liaoning Province (2022-BS-283), and Technology Liaoning Project Grants (601010326). Key projects supported by the Research Foundation of Education Bureau of Liaoning Province (No. JYTZD2023093), Distinguished Professor Project of Education Department of Liaoning and the Open Project Fund of Key Laboratory of Energy Materials and Electrochemistry Liaoning Province are acknowledged.

Notes and references

1 Z. W. Seh, Y. Sun, Q. Zhang and Y. Cui, *Chem. Soc. Rev.*, 2016, **45**, 5605–5634.
2 J. Sivaraj, B. Dasari and K. Ramesha, *Energy Fuels*, 2023, **37**, 9672–9681.
3 N. Nakamura, S. Ahn, T. Momma and T. Osaka, *J. Power Sources*, 2023, **558**, 232566.
4 L. Cai, H. Ying, P. Huang, Z. Zhang, H. Tan, Q. Han and W. Q. Han, *Chem. Eng. J.*, 2023, **474**, 145862.
5 M. Chen, W. Xu, S. Jamil, S. Jiang, C. Huang, X. Wang, Y. Wang, H. Shu, K. Xiang and P. Zeng, *Small*, 2018, **14**, 1803134.
6 H. Yang, P. Chen, W. Chen, K. Li, M. Xia, H. Xiao, X. Chen, Y. Chen, X. Wang and H. Chen, *Fuel Process. Technol.*, 2022, **230**, 107215.
7 Z. L. Xu, J. K. Kim and K. Kang, *Nano Today*, 2018, **19**, 84–107.
8 W. Sun, Z. Song, Z. Feng, Y. Huang, Z. J. Xu, Y. C. Lu and Q. Zou, *Nano-Micro Lett.*, 2022, **14**, 222.
9 J. Luo, K. Guan, W. Lei, S. Zhang, Q. Jia and H. Zhang, *J. Mater. Sci. Technol.*, 2022, **122**, 101–120.
10 X. Gao, C. Zheng, Y. Shao, V. R. Shah, S. Jin, J. Suntivich and Y. L. Joo, *ACS Appl. Mater. Interfaces*, 2023, **15**, 19011–19020.
11 Y. Qi, N. Chai, Q. Gu, J. Chen, M. Lu, X. Zhang and B. Zhang, *Chem. Eng. J.*, 2022, **435**, 135112.
12 Y. Wen, Z. Shen, J. Hui, H. Zhang and Q. Zhu, *Adv. Energy Mater.*, 2023, **13**, 2204345.
13 S. A. Abbas, J. Ding, S. H. Wu, J. Fang, K. M. Boopathi, A. Mohapatra, L. W. Lee, P.-C. Wang, C.-C. Chang and C. W. Chu, *Acs Nano*, 2017, **11**, 12436–12445.
14 J. Wang and W.-Q. Han, *Adv. Funct. Mater.*, 2022, **32**, 2107166.
15 S. Deng, T. Guo, J. Heier and C. Zhang, *Adv. Sci.*, 2023, **10**, 2204930.
16 H. Wang, C. Xu, X. Du, G. Liu, W. Han and J. Li, *Chem. Eng. J.*, 2023, **471**, 144338.
17 L. Fan, M. Li, X. Li, W. Xiao, Z. Chen and J. Lu, *Joule*, 2019, **3**, 361–386.
18 J. Wang, T. Gan, Y. Liao, F. Wu, Z. Lin and G. Ai, *J. Alloys Compd.*, 2023, **960**, 170546.
19 M. Xu, P. Dong, T. Li, H. Hua, Y. Li, X. Li, Y. Zhang, Y. Zhang and J. Zhao, *Appl. Surf. Sci.*, 2020, **504**, 144463.
20 D. Yang, C. Zhang, J. J. Biendicho, X. Han, Z. Liang, R. Du, M. Li, J. Li, J. Arbiol and J. Llorca, *ACS Nano*, 2020, **14**, 15492–15504.
21 C. Ye, L. Zhang, C. Guo, D. Li, A. Vasileff, H. Wang and S. Z. Qiao, *Adv. Funct. Mater.*, 2017, **27**, 1702524.
22 Y. Wu, D. Li, J. Pan, Y. Sun, W. Huang, M. Wu, B. Zhang, F. Pan, K. Shi and Q. Liu, *J. Mater. Chem. A*, 2022, **10**, 16309–16318.
23 Y. Wang, Y. Xiong, Q. Huang, Z. Bi, Z. Zhang, Z. Guo, X. Wang and T. Mei, *J. Mater. Chem. A*, 2022, **10**, 18866–18876.
24 S. Huang, Z. Wang, Y. Von Lim, Y. Wang, Y. Li, D. Zhang and H. Y. Yang, *Adv. Energy Mater.*, 2021, **11**, 2003689.
25 T. Zhou, X. Yu, F. Li, J. Zhang, B. Liu, L. Wang, Y. Yang, Z. Hu, J. Ma, C. Li and G. Cui, *Energy Storage Mater.*, 2023, **55**, 691–697.
26 Z. Wei, C. Liang, L. Jiang, L. Wang, S. Cheng, Q. Peng, L. Feng, W. Zhang, J. Sun and Q. Wang, *Energy Storage Mater.*, 2022, **47**, 51–60.
27 N. Li, L. Yu, J. Yang, B. Zheng, X. Qiu and J. Xi, *Nano Energy*, 2021, **79**, 105466.
28 D. Su, M. Cortie and G. Wang, *Adv. Energy Mater.*, 2017, **7**, 1602014.
29 X. Dai, G. Lv, Z. Wu, X. Wang, Y. Liu, J. Sun, Q. Wang, X. Xiong, Y. Liu and C. Zhang, *Adv. Energy Mater.*, 2023, **13**, 2300452.
30 B. Yan, Y. Li, L. Gao, H. Tao, L. Zhang, S. Zhong, X. Li and X. Yang, *Small*, 2022, **18**, 2107727.
31 Y. Huang, L. Lin, Y. Zhang, L. Liu, B. Sa, J. Lin, L. Wang, D.-L. Peng and Q. Xie, *Nano-Micro Lett.*, 2023, **15**, 67.
32 Z. Liu, M. Chen, D. Zhou and Z. Xiao, *Adv. Funct. Mater.*, 2023, **33**, 2306321.
33 C. Jin, L. Zhou, L. Fu, J. Zhu, D. Li and W. Yang, *J. Power Sources*, 2017, **352**, 83–89.
34 Y. V. Lim, S. Vafakhah, X. L. Li, Z. Jiang, D. Fang, S. Huang, Y. Wang, Y. S. Ang, L. K. Ang and H. Y. Yang, *Small Sci.*, 2023, **3**, 2300070.

